**THE EUROPEAN
PHYSICAL JOURNAL B**

Pressure-induced structural transition in amorphous GeO$_2$: a molecular dynamics simulation

Joaquín Peralta[1,a] and Gonzalo Gutiérrez[2]

[1] Departamento de Física, Facultad de Ciencias Exactas, Universidad Andrés Bello, Santiago, Chile
[2] Departamento de Física, Facultad de Ciencias, Universidad de Chile, Casilla 653, Santiago, Chile

Abstract. We studied the structural and dynamical properties of amorphous germanium dioxide (GeO$_2$) from low to high pressure by means of the classical molecular dynamics technique. The simulations were done in the micro-canonical ensemble, with systems at densities ranged from 3.16 to 6.79 g/cm^3, using a pairwise potential. The network topology of the systems is analyzed at atomic level through partial pair correlations, coordination number and angular distributions. The dynamic properties were characterized by means of the vibrational density of states. According the density increases, a structural transformation from a short-range order, defined by a building block composed by a basic (GeO$_4$) tetrahedron, to a basic (GeO$_6$) octahedron is observed. The vibrational density of states also presents important changes when the density increases, with a low frequency band lessened, and a high density band wider and flatter.

1 Introduction

GeO$_2$, also known as *germania*, has been studied extensively during last years both by experiments [1–3] as well as by means of computer simulations, mainly classical and ab initio molecular dynamics, in its crystalline, liquid and amorphous phases [4–10]. Germania is a structural and chemical analog to silica, SiO$_2$, showing interesting differences and similarities at normal and high pressure [11]. Although germania has not as much practical applications as silica [12,13], it stands out as an optical material, and has been used in wide-angle lenses and in microscopy as optical objective lenses [14,15]. The mixture of silica and germania is used as a material for optical fibers and waveguides [16,17], which under concentration control could regulate the refractive index [18]. In its crystalline state, germania has two phases: a low density phase, where – like silica – adopts an α-quartz structure with tetrahedrally coordinated germanium, and a high density phase, with a rutile-like structure, with six-fold coordination of germanium.

Both germania and silica are archetypal oxide, strong glass forming material [19], characterized, at room conditions, by a tetrahedral network of A(O$_{1/2}$)$_4$ (A = Si, Ge) apex-bridged tetrahedra joined to each other by oxygen atoms. These tetrahedra are randomly oriented, linked by their vertices with a broad distribution of A-O-A angles, resulting in a three-dimensional structure possessing a medium range order [20,21]. Interestingly, from both the applied and fundamental point of view, there has been considerable attention to the behavior of these amorphous materials under pressure because the structural and dynamical changes that take place. In the case of germania, this structural change can be related to the to anomalous behavior in its elastic, thermal and viscous properties, as well as in the polyamorphism observed [10,22–24]. In fact, it has been established that when submitted to high pressure, both systems (germania and silica) present a structural transition from a tetrahedral to an octahedral A(O$_{1/3}$)$_6$ network, which implies a large change in density and in the short and medium range order [25]. But in contrast to amorphous silica, where such transformation is ranged above 10 GPa [11], for amorphous germania it takes place above 3 GPa, which is more manageable in actual experiments [11,26–29]. In this study we assess the phenomena of the phase transition for amorphous GeO$_2$ by the use of classical molecular dynamics technique and a simple pair-potential model.

Classical molecular dynamics technique has played a fundamental role in the study and characterization of the GeO$_2$ phases at a variety of conditions (e.g. liquid, solid, and molten state; both normal and high pressure) [5,7,8,30,31], and has been helpful in revealing atomic level characteristics of the structure and the dynamics of the GeO$_2$. In this work we studied the amorphous phase of GeO$_2$ at pressures ranging approximately from 0 to 40 GPa by classical molecular dynamics technique, using a Buckingham type pairwise potential. The results presented are the structural and vibrational properties for 26 different densities. In contrast to previous

a e-mail: joaquin.peralta@unab.cl

simulations, as the work of Marrocchelli et al. [10], which use a much more sophisticated and time consuming potential [28,32], we perform our calculations using the pair potential proposed by Oeffner and Elliott [33] mainly motivated for the simplicity. In that paper, Oeffner and Elliott present two different sets of parameters: one fitted from an ab initio energy surface, and a so-called rescaled one, which was developed from the previous one in order to give a better reproduction of the vibrational properties. Interestingly, the rescaled Oeffner and Elliott potential was already used for amorphous GeO_2 at normal pressure, presenting a good agreement in the structural and vibrational properties to the experimental results [31]. In addition, it is also comparable in the vibrational density of states to the new potential proposed by Marrocchelli et al. [32]. Thus, our goal is to study, by means of a simple, yet reliable inter-atomic potential, the structural and vibrational properties of GeO_2 under pressure, and the interplay between the changes at the short and intermediate range order, and the vibrational spectra.

This paper is organized as follows. After this introduction, in Section 2 we provide details of the MD simulation and the preparation of the amorphous state of the GeO_2 at different densities. Results of the structural and vibrational properties, along with the short-range order and network topology are presented in Section 3. A discussion of our findings is given in Section 4.

2 Methodology

The molecular dynamics study has been done using an orthogonal cell with 576 atoms (192 Ge + 384 O) under periodic boundary conditions. It has been shown that a larger number of atoms is not necessary for this particular case [31]. The system was analyzed preparing 26 different samples at densities from $\rho = 3.16$ g/cm^3 to $\rho = 6.79$ g/cm^3, where the density at room condition ($\rho = 3.70$ g/cm^3[34]) is located in between that range. The force field to describe the inter-atomic interactions is the one developed by Oeffner and Elliott [33]. The potential has a Buckingham functional form, and has been demonstrated that reproduce a considerable number of experimental properties for the crystalline and amorphous phases, such as structure, density, bulk modulus, thermal expansivities and melting temperatures among others [30,31,33]. In addition, this potential shows a good agreement with vibrational and structural properties of *germania* at room temperature and pressure [31]. This potential employs pairwise additive inter-atomic terms of the form

$$V(r_{ij}) = \frac{q_i q_j}{r_{ij}} - \frac{A_{ij}}{r_{ij}^6} + B_{ij} \exp\left(-C_{ij} r_{ij}\right), \qquad (1)$$

where r_{ij} is the inter-atomic distance between atoms i and j. The effective charge $q_{(i,j)}$, the van der Waals coefficients A_{ij}, the softness parameter B_{ij} and the repulsive radius C_{ij}, are the energy parameters, which are displayed in Table 1 and correspond to the rescaled potential described by Oeffner and Elliott. The long range Coulomb

Table 1. Potentials parameters, using $q_{Ge} = 0.94174$ and $q_O = -0.47087$. These values correspond to the rescaled potential parameters of Oeffner and Elliott [33].

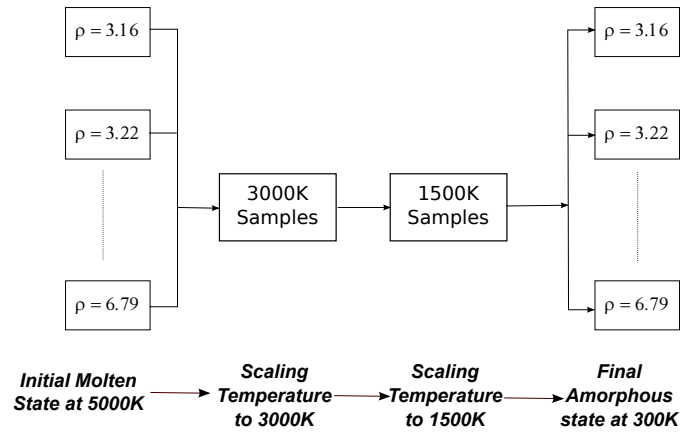|	A_{ij} (kJ Å^{-6} mol^{-1})	B_{ij} (kJ mol^{-1})	C_{ij} (Å^{-1})
Ge–Ge	0	0	0
Ge–O	2.2833×10^4	2.00696×10^7	6.12933
O–O	1.2648×10^4	7.42295×10^5	3.28511

Fig. 1. General procedure for 26 different densities range between 3.16 and 6.79 g/cm^3 for GeO_2. We start with a melting state at 5000 K and after three different temperature scaling process we obtain the final samples at 300 K for each density.

interactions are calculated with the standard Ewald summation technique. The equations of motion are integrated with a modification of Beeman algorithm, as is implemented in the program MOLDY [35], using a time step $\Delta t = 1 \times 10^{-15}$ s.

Special attention was put in the preparation of the sample to avoid any cooling rate effects [36]. The procedure used to prepare the samples consists in the *quench-from-the-melt* technique, similar to the one described in reference [37], and is shown in Figure 1. The cooling rate as well the equilibration procedure were conducted by velocity rescaling method, after which the system evolved with no temperature control. Thus starting at densities in the initial molten state at 5000 K, each one is cooled to 3000 K using a cooling rate of -0.02 K$/\Delta t$. Then, by the use of velocity rescaling, the samples are equilibrated during $20\,000\Delta t$, and others $20\,000\Delta t$ with any disturbance. In the second step, the samples are cooled from 3000 K to 1500 K using a cooling rate of -0.0075 K$/\Delta t$, equilibrating them during the next $50\,000\Delta t$, and other $50\,000\Delta t$ with any disturbance. In the third and last step the samples are cooled to room temperature using a rate of -0.0024 K$/\Delta t$, applying a temperature control for the next $75\,000\Delta t$, and leaving without temperature control the last $75\,000\Delta t$ which correspond to the used data in every analysis in this work.

A pressure density phase diagram at room temperature of the resulting samples is presented in Figure 2, along with the experimental results of Hong et al. [38]. In spite of the difference of the precise values, a resemblance is
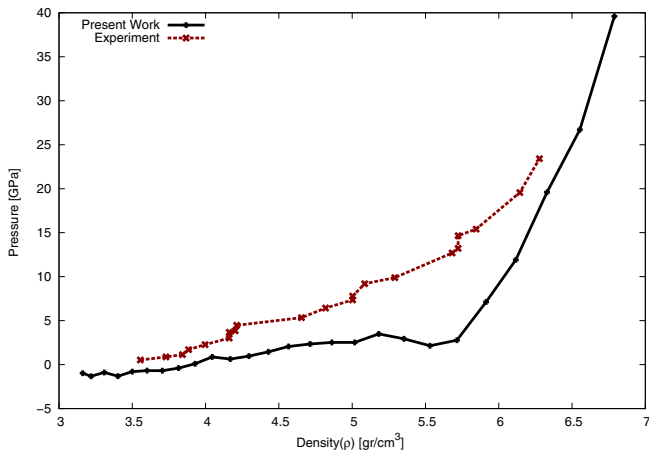
Fig. 2. P-ρ diagram for a temperature $T = 300$ K. Two principal branches are observed in the figure, below and above 5.5 g/cm^3 that denote different phases presence in the samples. Dashed line corresponds to experimental results of Hong et al. [38].
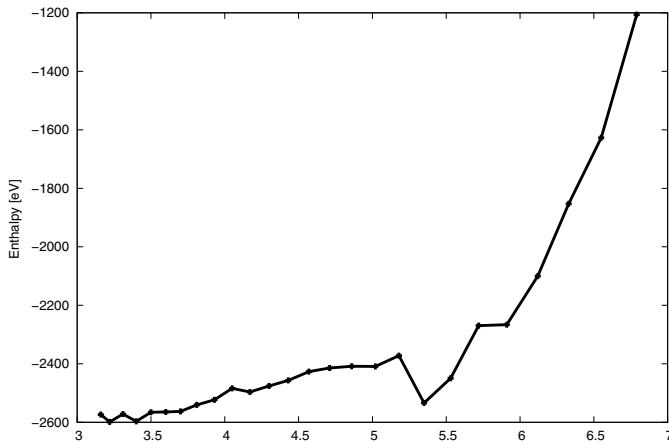

Fig. 3. Enthalpy diagram $H = U + PV$. Two main branches can be delimited by a density interval ranged between 5 and 6 g/cm^3.

Fig. 4. Pair Distribution Function (PDF) evaluated for Ge–O bond, Ge–Ge, and O–O distances, and the total PDF. A clear displacement of the first peak is observed for all cases according the pressure increases.

observed between them. It can be clearly seen two different behaviors. Below 5.5 g/cm^3 there is a slow increment of pressure according the density increases. But for densities greater than 5.5 g/cm^3 the P–ρ curve is steeper. As we will see, this two branches denote different structural arrangements, related to the building block of the glass, that changes from a GeO$_4$ to a GeO$_6$ basic unit, according pressure increases. Interestingly the enthalpy $H = U + PV$ plot (see Fig. 3) stressed the two different regimes according the density increases, which can be localized between 5 and 6 g/cm^3, that corresponds to pressures close to 3 and 7 GPa, respectively. These results are in good agreement with the experimental work of Vaccari et al. [27] which localize a structural transition between 6 and 12 GPa. In the same sense, Marrochelli et al. [10] and recently Salmon et al. [28], reported that the change from GeO$_4$ to GeO$_6$ structures start at a similar range and the transition is not completed before 15 GPa.
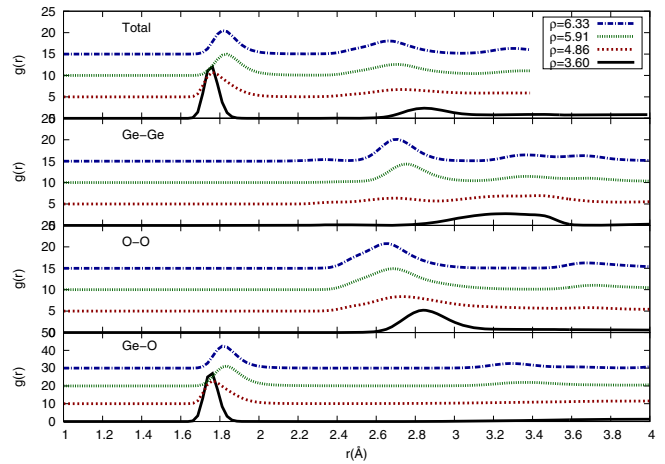
3 Results

After the 26 samples were obtained at room temperature, we performed a detailed analysis, both on the structural and vibrational properties, in order to describe the short and medium range order. The structural properties studied are pair distribution functions, coordination number, angular distribution function, and static structure factors. Vibrational properties, first reported at high pressure using computational simulations, give an interesting point of view about the atoms and structure frequencies. In what follows we present in detail only four representative densities: 3.6, 4.86, 5.91, and 6.33 g/cm^3 to characterize the structural and dynamical properties of GeO$_2$ in the main phases as well as in the transition. Analyses were done using the tools provided by LPMD package [39]. The densities chosen correspond to pressures of −0.68, 2.52, 7.12 and 19.60 GPa, respectively. Table A.1 presented in Appendix shows general results for each simulated density.

3.1 Structural properties

The pair distribution function $g_{\alpha\beta}(r)$ (PDF), is one of the basic structural analysis in the study of amorphous materials, giving us the probability of found neighbors of species β for a specific distance r of the atomic species α. Figure 4 shows the results of the total $g(r)$ and the partial Ge–O, O–O, and Ge–O PDF's at the four different densities. For the Ge–O bond distance, the first peak shifts from 1.72 Å to 1.82 Å, denoting a change in the short range order according the pressure is increased, in good agreement with the experimental results of Stone et al. [40] and the recent measurement of Vaccari et al. [27], and slightly different with respect to the ab initio work of Zhu and Chen [41]. However, our results also present a good agreement with the work of Marrochelli et al. [32] that uses a recent developed ab initio based potential for GeO$_2$.
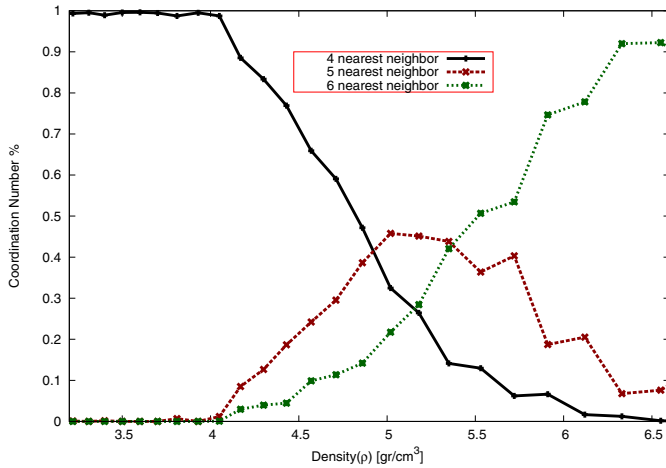
Fig. 5. Ge-O$_X$ concentration in the sample for $X = 4, 5,$ and 6. As density increases the number of GeO$_4$ (tetrahedron) decreases and the number of GeO$_6$ (octahedron) increases. The number of GeO$_5$ in the sample increases finding a maximum around 5.2 g/cm^3.

The O–O inter-atomic distance change from 2.84 Å (close to the tetrahedral type structure, $r_{\text{o-o}} = \sqrt{8/3}r_{\text{ge-o}}$) to 2.66 Å. The Ge–Ge interatomic distance at low pressure presents a wide peak around 3.3 Å changing to a sharper peak centered at 2.7 Å at high density. As we will see, this fact is related to a change in the inter-conection of the building block.

A useful complementary information is provided by the average coordination number $n_{\alpha\beta}$, given by:

$$n_{\alpha\beta}(R) = 4\pi\rho_\beta \int_0^R g_{\alpha\beta}(r)\, r^2\, dr, \qquad (2)$$

where R is a cutoff, usually chosen as the position of the minimum after the first peak of the partial distribution function $g_{\alpha\beta}(r)$. The coordination number informs the percentage of α atoms surrounded by n atoms β. The results, displayed in Figure 5, for a density increase from 4.5 g/cm^3 to 6.5 g/cm^3, show an important structural change in the percentage of GeO$_X$ polyhedra (for $X = 4, 5,$ and 6). Close to 5.3 g/cm^3 a crossing of GeO$_4$ and GeO$_6$ concentration curves is observed. The number of the GeO$_5$ structures in the sample increases initially and then decreases, presenting a maxima value close to 5.2 g/cm^3, near to the crossing of the GeO$_4$ and GeO$_6$ concentration, where the principal structural change occurs. Note this corresponds to the second regime observed by Salmon et al. [28] in their neutron diffraction experiment.

In the final stage of the transition from low to high density, the number of GeO$_6$ and GeO$_5$ in the sample is around 90% and 10%, respectively. These results are slightly different from the ones of the work of Ting et al. [42], where the concentration of GeO$_6$ is less than GeO$_5$. Unlike our work, Ting et al. use the non-scaled potential that propose Oeffner and Elliott [33], that could explain the differences. On the other hand, we present a best agreement with Micoulaut et al. [43] where the cross-
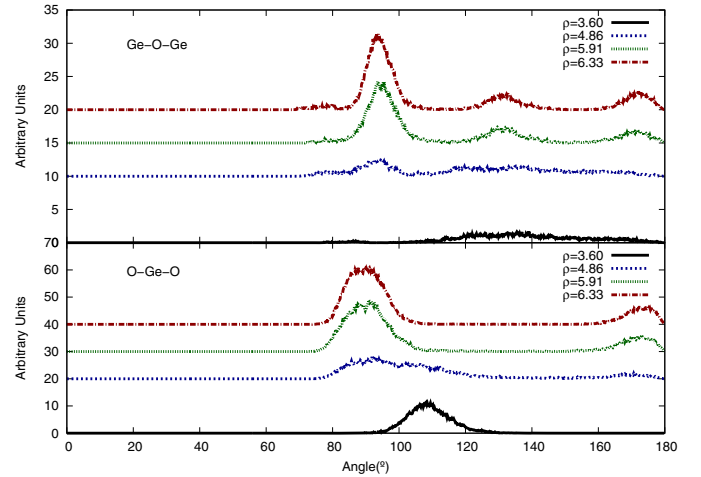

Fig. 6. Angles distribution function. The principal structural angles Ge–O–Ge and O–Ge–O are displayed.

ing occurs at some slightly smaller density. A reasonable agreement with ab initio work of Marrocchelli et al. [10] is also obtained, where the intersection between GeO$_6$ and GeO$_4$ is located at 5.5 g/cm^3. This suggests that a complete phase transformation must take place not before 15 GPa. A pressure of 15 GPa (which in turn corresponds to a density between 6.12 and 6.33 g/cm^3 and a concentration of 80−90% of GeO$_6$ structures in the sample, as is derived from Tab. A.1). Interestingly, according to our simulations, at pressures near 30 GPa, when the glass is composed mainly by an octahedral network, further densification proceeds via compression of Ge–O bonds: from a maximum of 1.84 Å in the range of 3 to 10 GPa, Ge–O distance decreases to 1.79 Å at 39.6 GPa (see Tab. A.1). This is the same behavior found in the experimental work of Salmon et al. [28].

Further information about the structural units is provided by the angular distribution function (ADF) which is defined as a histogram constructed for angles A–B–C, where A, B, and C correspond to three atomic species, B being the central atom. Figure 6 shows the results of two principal angles of the sample. The angle O–Ge–O changes from ∼109° at 3.6 g/cm^3 to ∼90° at 6.33 g/cm^3 is related to the internal structure of the building block tetrahedron GeO$_X$. On the other hand, Ge–O–Ge angle is related to the inter-polyhedra link, and has a broader distribution centered at ∼130° at low density, and shifts to ∼93° at high density.

With all the previous information, we identify the main structural change that occurs in the basic structure of the *germania*, which consists in a transition from a GeO$_4$ tetrahedral basic building block to an GeO$_6$, octahedral one, according the density is increased. The structural change has been established between 5 and 6 g/cm^3 densities, that correspond to pressures of 3–7 GPa, respectively. Figure 7 shows the atomic structures for such basic structures.

The molecular dynamics results can be directly compared to experiment by obtaining the scattering static structure factor, both for neutron and X-ray at normal and
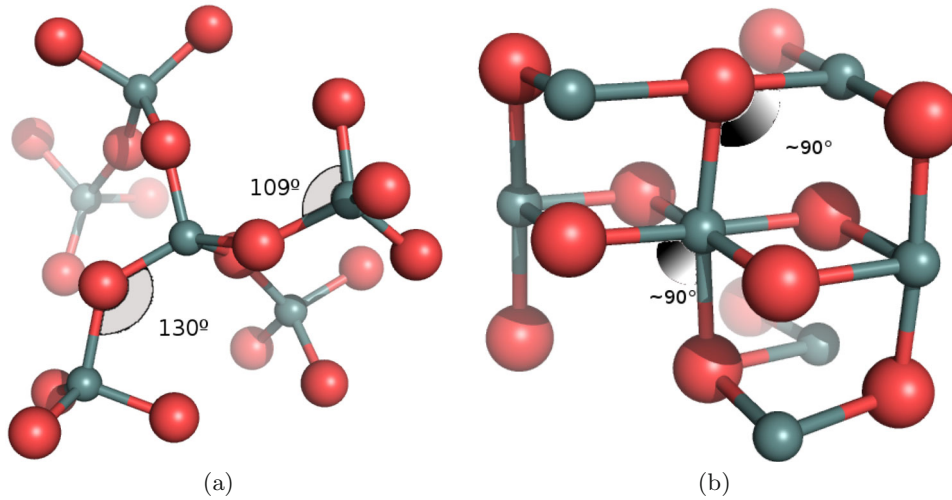
Fig. 7. Basic brick structure of amorphous GeO$_2$ at normal (a) and high (b) pressure, both are extracted from the simulation cell. A clear structural change that shows the phase transformation from tetrahedral like the fundamental structure to octahedral as a new one at high pressure.

high pressure conditions. The partial static structure factors are calculated from the Fourier transform of the corresponding partial pair distribution functions by means of

$$S_{\alpha\beta}(q) = \delta_{\alpha\beta} + 4\pi\rho(c_\alpha c_\beta)^{1/2}$$

$$\times \int_0^R r^2[g_{\alpha\beta}(r) - 1]\frac{\sin(qr)}{qr}\frac{\sin(\pi r/R)}{\pi r/R}dr, \quad (3)$$

where $c_{\alpha(\beta)} = N_{\alpha(\beta)}/N$ is the concentration of α (β) species. The window function $\frac{\sin(\pi r/R)}{\pi r/R}$ has been introduced to reduce the termination effects resulting from the finite upper limit [44]. The cutoff length, R, is chosen to be half the length of the simulation box. The results are presented in Figure 8. For all densities, the main contribution from the Ge–Ge correlation come from the first peak, and then from others correlations (Ge–O, and O–O). According the density is increased the first peak begins to disappear, mainly because there are almost no Ge–O and O–O correlations, and the Ge–Ge is decreasing. The origin of the second peak can be found in the Ge–Ge and O–O correlations and the partial cancellation arising from Ge–O anti-correlation. This negative correlation appears because, although GeO$_2$ is a covalent glass, there is also present some ionic character and there exist charge transfer effects. When the pressure starts to increase, the second peak of the O–O correlation increases considerably and slowly is displaced to greater values of q, while the Ge–Ge and O–O correlations, despite the increase in value, do not shift. Finally, the third peak is due to all the three correlations and when the pressure is increased this peak become sharper and well defined.

All the previous information gives us a fingerprint about the real space correlation [45], and like at the silica case [46], we can associate every peak to the different range order of the sample. The first peak corresponds to the so-called First Sharp Diffraction Peak (FSDP) q_{FSDP}.
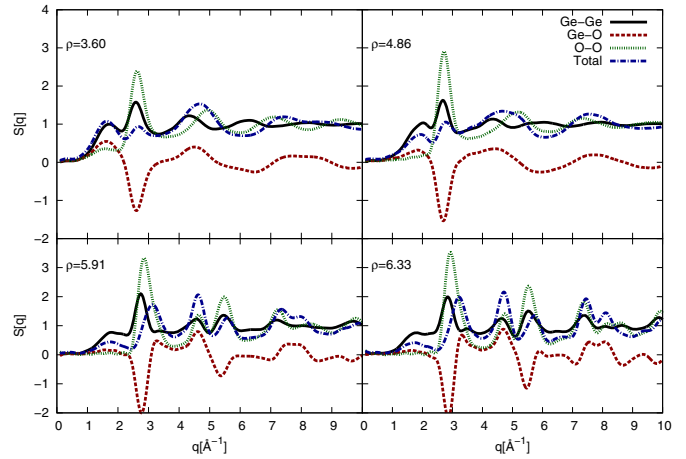

Fig. 8. Partial structure factors, at four different densities, for the amorphous GeO$_2$ structure. The information of the first three peaks, gives us a real-space fingerprint of the structure.

The FSDP is a feature that appears in a variety of binary covalent glasses, including GeO$_2$, SiO$_2$, SiSe$_2$, As$_2$Se$_3$, As$_2$S$_3$, etc., and is related to the intermediate range order of the glass.

The FSDP presents a displacement according the density is increased from $\sim$1.67 Å^{-1} to $\sim$1.76 Å^{-1}. The intermediate range order have a periodicity in the real space of $2\pi/q_{FSDP}$ between 3.76 Å and 3.57 Å. That is directly related to the distance between tetrahedra and octahedra in the simulation-cell. These distances are beyond the second neighbors, presented in the total PDF. The second peak of the partial structure factor is located at $\sim$2.70 Å^{-1} at normal density and is displaced to $\sim$3.18 Å^{-1} at high density. These values are related to the correlation of the real space with $2\pi/q$ with values of 2.33 Å and 1.98 Å, respectively. These values correspond to an intermediate
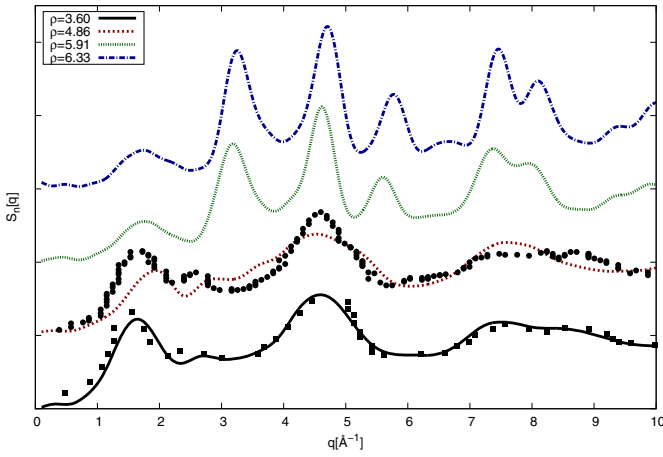
Fig. 9. Neutron structure factors at four different densities. The three main peaks are displaced in order the density is increased. A reasonable agreement is observed at room conditions with the experimental results of Drewitt et al. [3] (black squares). The comparison of the curve at $\rho = 4.86$ g/cm^3 is presented with the experimental results of Drewitt et al. at a pressure of 3.1 GPa (black circles). A displacement of the first two peaks is observed in comparison with experimental data.

distance between first and seconds neighbors. The positions give a characteristic distance of how the tetrahedron and octahedron are linked each other. Finally, the third peak give us information about the short-range order in the real space, and is related to the basic tetrahedral and octahedral structures at different pressures. The third peak is located at ~4.61 Å^{-1} to low density and displaced to ~4.70 Å^{-1} to high density. At low density it is wider and flatter and at high density become sharper and well defined. The related values in the real space correspond to 1.36 Å and 1.34 Å respectively. The values that are close to half-way between first neighbors are related to the internal structure of the octahedron and tetrahedron.

The neutron scattering static structure factor can be obtained from the partial static structure factors by weighting them with the coherent neutron-scattering lengths:

$$S_N(q) = \frac{\sum_{\alpha\beta} b_\alpha b_\beta \, (c_\alpha c_\beta)^{1/2} [S_{\alpha\beta}(q) - \delta_{\alpha\beta} + (c_\alpha c_\beta)^{1/2}]}{\left(\sum_\alpha b_\alpha c_\alpha\right)^2} \quad (4)$$

where b_α denotes the coherent neutron scattering length of species α. We use $b_{\mathrm{Ge}} = 0.8193 \times 10^{-4}$ Å and $b_{\mathrm{O}} = 0.5805 \times 10^{-4}$ Å [47]. The calculated $S_N(q)$ curves are presented in Figure 9 and compared with recent experimental results of Drewitt et al. [3]. For a clear view, the curves has been displaced vertically for each different density. Three principal peaks are observed in the region defined between $0 < q < 5$ Å^{-1}, changing their shapes according the density is increased. The first peak, located at 1.65 Å^{-1} for the low density sample, is displaced to 1.80 Å^{-1} at high density, becoming wider. The second peak, poorly defined at low density, becomes sharp at high density, shifting from $q = 2.71$ Å^{-1} to $q = 3.36$ Å^{-1}. The third peak shows a displacement from $q = 4.63$ Å^{-1} to $q = 4.84$ Å^{-1}, becom-
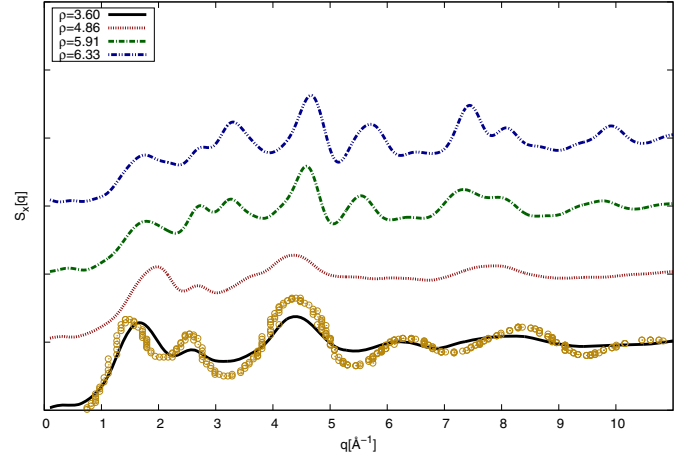

Fig. 10. X-ray structure factors at four different densities. A peak new fourth peak emerge here in order the density is increased. This fact is due to the two body charge-charge correlation. The golden circles correspond to the experimental results for amorphous germania at room conditions by Drewitt et al. [3].

ing sharper and well defined according pressure increases. Our results for $\rho = 4.86$ g/cm^3 are compared with the experimental pressure of 3.1 GPa of Drewitt et al. [3] because that density corresponds approximately to pressure of ~3 GPa (see Tab. A.1).

Similar to the previous procedure mentioned above, the X-ray diffraction factor is obtained by:

$$S_X(q) = \frac{\sum_{\alpha,\beta} f_\alpha(q) f_\beta(q) \, (c_\alpha c_\beta)^{1/2} \, S_{\alpha\beta}(q)}{\sum_\alpha f_\alpha^2(q) c_\alpha}, \quad (5)$$

where $f_\alpha(q)$ is the q-dependent X-ray form factor, given by:

$$f_\alpha(q) = \sum_{i=1}^4 a_{\alpha,i} \exp[-b_{\alpha,i}(q/4\pi)^2] + c_\alpha. \quad (6)$$

Parameters $a_{\alpha,i}$, $b_{\alpha,i}$ and c_α are taken from [48] for germanium and [49] for oxygen. The results are presented in Figure 10 along with experimental data from Drewitt et al. [3] at room conditions. As in neutron structure factor, three peaks are defined in the region between $0 < q < 5$ Å^{-1} at low density which show a reasonable agreement with the experimental results. But at high density $\rho = 6.33$ g/cm^3, four peaks can be distinguished in that region. This feature, only present in X-ray diffraction pattern, becomes apparent following what happens at intermediate densities. The first peak behaves in a similar way that S_N: displaced from 1.49 Å^{-1} to 1.59 Å^{-1}, becomes less defined according the density increased. The third peak shows a small displacement to higher values of q and becomes sharper as density increases. Note that two peaks are observed between the first and third peaks at the highest density curve. The one at lower q (2.35 Å^{-1}) value come from the second peak of the low density curve (2.45 Å^{-1}). On the other hand, the other peak in the high density curve (2.99 Å^{-1}) emerge only due to the changes in density, as is shown by the small hump at 4.8 g/cm^3. This fact
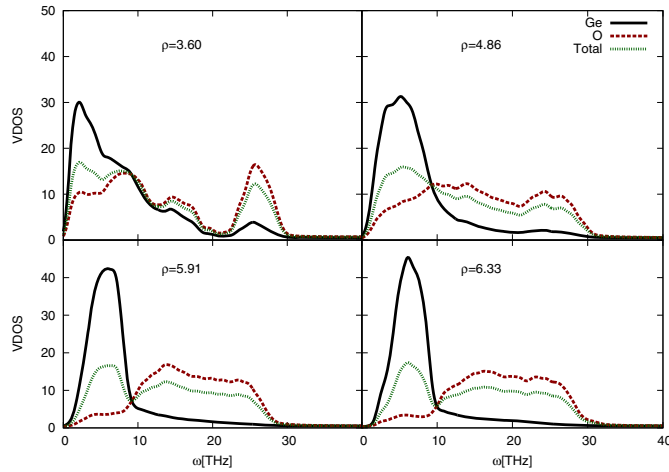
Fig. 11. Vibrational Density of States at four different densities. The total VDOS at lower densities show a wider low frequency band, unlike high density, where a narrower low frequency band is observed.

is due to the two body charge-charge correlation, taken into account in the X-ray diffraction pattern, and absent in the density-density static structure factor $S(q)$.

3.2 Vibrational properties

The vibrational properties of amorphous GeO_2 have been characterized by means of the Vibrational Density of States (VDOS). The VDOS is obtained by using the Velocity Autocorrelation Function (VACF),

$$Z_{\alpha(\beta)}(t) = \left\langle \sum_{i=1}^{N} m_{i\alpha} \boldsymbol{v}_{i\alpha}(0) \cdot \boldsymbol{v}_{i\alpha}(t) \right\rangle, \qquad (7)$$

where $m_{i\alpha(\beta)}$ and $v_{i\alpha(\beta)}$ correspond to the mass and velocity of the atom i of the involved species α, β, respectively. The symbol $\langle \dots \rangle$ indicates temporal average over configurations. The Fourier transform of VACF gives us the VDOS for different species involved in the simulation. The partial VDOS, $\mathcal{D}_{\alpha(\beta)}$, is given by:

$$\mathcal{D}_{\alpha(\beta)}(\omega) = \frac{1}{\sqrt{2\pi}} \int \frac{Z_{\alpha(\beta)}(t)}{Z_{\alpha(\beta)}(0)} \exp\left(-i\omega t\right) dt. \qquad (8)$$

The total VDOS, $\mathcal{D}(\omega)$ is obtained by means of $\mathcal{D}(\omega) = \sum_{\alpha} c_{\alpha} \mathcal{D}_{\alpha}(\omega)$.

In Figure 11 are presented the VDOS corresponding to the four main densities. In all cases there are common features: the VDOS range from 0 to 30 THz and two frequency bands can be distinguished, a lower and a higher band. In our case, the lower band is mainly due to Ge atom vibrations, whereas the higher band to O atom vibrations, as can be deduced from the contribution of partial VDOS. This picture is consistent to what has been observed in covalent glasses, where the network is composed by basic building blocks (like GeO_4 tetrahedra at low density or GeO_6 octahedra at high density) linked each other; in these cases, the lower band is related to inter basic-block

bond-bending modes and the high band is related to the intra basic-block bond-stretching modes [8,31,50,51]. At the lowest density, the lower band extend up to 20 THz, and the higher band has a characteristic and well defined peak around 25 THz. According the density is increased, a modification of the VDOS is observed. At the highest density, the lower band decreases its range, reaching only up to 10 THz, but presenting a clear peak due mainly to Ge contribution. On the other hand, the high frequency band now becomes flatter and wider (from 10 to 30 Thz). In between these two densities (i.e. in between 3.6 and 6.33 g/cm^3), practically the distinction of the lower and higher frequency bands disappear, reflecting the fact that the network is composed, in addition to tetrahedra and octahedra, also by GeO_5 basic structures, all of them in similar proportions. The changes observed in the VDOS can be correlated with the behavior of the static structure factor $S(q)$. For instance, the first sharp diffraction peak (FSDP) present in the $S(q)$ at low pressure, disappears at high pressure. The FSDP is the fingerprint of the intermediate range order, that is, the existence of coherent structures larger than 15 Å. Consistent to this picture, in the VDOS we observe a shift to higher values of ω of the Ge curve peak at the low frequency band, according the pressure increase. That is because the peak was due to the vibration of these coherent structures that conform the intermediate range order.

4 Conclusions

In the present work, we have presented an atomistic simulation on the physical changes of amorphous germania under pressure. We employed a pairwise interatomic potential proposed by Oeffner and Elliott, which is simple but yet it is able to reproduce the main features of the amorphous-amorphous transition presented in vitreous germania. Detailed analysis of the inter-atomic distance, angle distribution and coordination number of the amorphous GeO_2 sample allows us to determine that the short range order is defined by slightly distorted tetrahedra at low density and by octahedral structures at high density. In both cases these basic building-block structures are linked between them mainly by corners and edges, but also by faces.

The main structural changes in amorphous GeO_2 occur, according our results, around 3–7 GPa, changing from a network composed basically of GeO_4 tetrahedra to a one composed of GeO_6 octahedra. This conclusion is in good agreement with recent experimental and simulation works. The analysis of the vibrational properties reinforces these results, where two main frequency bands are observed: a low frequency associated to inter-tetrahedra (octahedra) vibration at low (high) density, and a high frequency band, associated to intra-tetrahedron (octahedron) vibration at low (high) density, mainly due to oxygen atoms vibrations. At high density the low frequency band shows a clear peak, and the high frequency band becomes flatter and wider.

Table A.1. Density, bond length, bond angle, Ge–O–Ge angle and bulk modulus of *germania*. Some special values are defined in a range because are not possible determine the exact value.

Phase	Density (g/cm^3)	Bond length (Å)	Ge–O coordination number	O–Ge–O angle	Ge–O–Ge angle	Bulk pressure (GPa)
	6.79	1.79	5.86	89.46	93.60	39.6
	6.55	1.81	5.92	90.54	92.88	26.7
	6.33	1.81	5.91	90.54	93.60	19.6
	6.12	1.84	5.76	91.80	93.60	11.9
	5.91	1.84	5.68	91.26	93.60	7.12
	5.72	1.81	5.47	91.62	95.22	2.77
	5.53	1.84	5.38	91.62	94.68	2.14
	5.35	1.84	5.28	92.16	95.22	2.93
	5.18	1.79	5.02	90.00	94.68	3.49
	5.02	1.79	4.89	91.62	92.52	2.52
	4.86	1.76	4.67	92.34	94.32	2.52
	4.71	1.76	4.52	92.88	129.96	2.34
	4.57	1.76	4.44	104.58	(94–137)	2.06
Amorph.	4.43	1.76	4.27	107.28	125.82	1.45
	4.30	1.76	4.21	107.28	138.24	0.964
	4.17	1.76	4.14	105.84	133.02	0.630
	4.05	1.76	4.01	106.02	(124–132)	0.875
	3.93	1.76	3.99	106.02	132.48	0.096
	3.81	1.76	4.00	107.46	(120–140)	−0.402
	3.70	1.76	3.99	108.72	(120–140)	−0.688
	3.60	1.76	4.00	108.00	135.72	−0.686
	3.50	1.76	4.00	108.72	129.06	−0.789
	3.40	1.76	3.99	108.36	135.90	−1.310
	3.31	1.76	3.99	108.00	131.40	−0.891
	3.22	1.76	3.99	106.20	139.14	−1.320
	3.16	1.76	3.99	108.72	(120–140)	−0.973

Appendix A: Results of all 26 different densities

This Appendix shows information of the results obtained for all different densities simulated, between 3.16 and 6.79 g/cm^3.

References

1. P. Salmon, A. Barnes, R. Martin, G. Cuello, J. Phys.: Condens. Matter **19**, 22 (2007)
2. Q. Mei, S. Sinogeikin, G. Shen, S. Amin, J. Benmore, K. Ding, Phys. Rev. B **81**, 174113 (2010)
3. J.W.E. Drewitt, P.S. Salmon, A.C. Barnes, S. Klotz, H.E. Fischer, W.A. Crichton, Phys. Rev. B **81**, 014202 (2010)
4. T. Tsuchiya, T. Yamanaka, M. Matsui, Phys. Chem. Miner. **27**, 149 (2000)
5. G. Gutiérrez, J. Rogan, Phys. Rev. E **69**, 031201 (2004)
6. S. Ono, T. Tsuchiya, K. Hirose, Y. Ohishi, Phys. Rev. B **68**, 134108 (2003)
7. M. Micoulaut, Y. Guissani, B. Guillot, Phys. Rev. E **73**, 031504 (2006)
8. L. Giacomazzi, P. Umari, A. Pasquarello, Phys. Rev. B **74**, 155208 (2006)
9. T. Li, S. Huang, J. Zhu, Chem. Phys. Lett. **471**, 253 (2009)
10. D. Marrocchelli, M. Salanne, P.A. Madden, J. Phys.: Condens. Matter **22**, 152102 (2010)
11. V.P. Prakapenka, G. Shen, L. Dubrovinsky, M. Rivers, S.R. Sutton, J. Phys. Chem. Solids **65**, 1537 (2004)
12. K. Muralidharan, J. Simmons, P. Deymier, K. Runge, J. Non-Cryst. Solids **351**, 1532 (2005)
13. A. Walcarius, Electroanalysis **10**, 1217 (1998)
14. D.G. Chen, B. Potter, J. Simmons, J. Non-Cryst. Solids **178**, 135 (1994)
15. C. Dalle, P. Cordier, C. Depecker, P. Niay, P. Bernage, M. Douay, J. Non-Cryst. Solids **260**, 83 (1999)
16. J. Ballato, T. Hawkins, P. Foy, S. Morris, N.K. Hon, B. Jalali, R. Rice, Opt. lett. **36**, 687 (2011)
17. V. Mizrahi, P.J. Lemaire, T. Erdogan, W.A. Reed, D.J. DiGiovanni, R.M. Atkins, Appl. Phys. Lett. **63**, 1727 (1993)
18. S. Uehara, K. Momono, Optical glass, US Patent 8, 207,075 (2012) http://www.google.com/patents/US8207075
19. M.I. Ojovan, W.B.E. Lee, J. Non-Cryst. Solids **356**, 2534 (2010)
20. S. Kohara, K. Suzuya, J. Phys.: Condens. Matter **17**, S77 (2005)
21. M. Micoulaut, A. Kachmar, T. Charpentier, Phys. Stat. Sol. B **249**, 1890 (2012)
22. C.A. Angell, P.H. Poole, J. Shao, Il Nuovo Cimento D **16**, 993 (1994)

23. R.L. Parc, C. Levelut, J. Pelous, V. Martinez, B. Champagnon, J. Phys.: Condens. Matter **21**, 079802 (2008)
24. M. Agarwal, A. Ganguly, C. Chakravarty, J. Phys. Chem. B **113**, 15284 (2009)
25. K.H. Smith, E. Shero, A. Chizmeshya, G.H. Wold, J. Chem. Phys. **102**, 6851 (1995)
26. D.J. Durben, G.H. Wolf, Phys. Rev. B **43**, 2355 (1991)
27. M. Vaccari, G. Aquilanti, S. Pascarelli, O. Mathon, J. Phys.: Condens. Matter **21**, 145403 (2009)
28. P.S. Salmon, J.W.E. Drewitt, D.A.J. Whittaker, A. Zeidler, K. Wezka, C.L. Bull, M.G. Tucker, M.C. Wilding, M. Guthrie, D. Marrocchelli, J. Phys.: Condens. Matter **24**, 439601 (2012)
29. K. Wezka, P.S. Salmon, A. Zeidler, D.A.J. Whittaker, J.W.E. Drewitt, S. Klotz, H.E. Fischer, D. Marrocchelli, J. Phys.: Condens. Matter **24**, 502101 (2012)
30. T. Tsuchiya, T. Yamanaka, M. Matsui, Phys. Chem. Miner. **25**, 94 (1998)
31. J. Peralta, G. Gutiérrez, J. Rogan, J. Phys.: Condens. Matter **20**, 145215 (2008)
32. D. Marrocchelli, M. Salanne, P. Madden, C. Simon, P. Turq, Mol. Phys. **107**, 443 (2009)
33. R. Oeffner, S. Elliott, Phys. Rev. B **58**, 14791 (1998)
34. O.B. Tsiok, V.V. Brazhkin, A.G. Lyapin, L.G. Khvostantsev, Phys. Rev. Lett. **80**, 999 (1998)
35. K. Refson, Comput. Phys. Commun. **126**, 310 (2000)
36. K. Vollmayr, W. Kob, K. Binder, Phys. Rev. B **54**, 15808 (1996)
37. Y. Liang, C. Miranda, S. Scandolo, High Press. Res. **28**, 35 (2008)
38. X. Hong, G. Shen, V. Prakapenka, M. Newville, M. Rivers, S. Sutton, Phys. Rev. B **75**, 104201 (2007)
39. S. Davis, C. Loyola, F. Gonzalez, J. Peralta, Comput. Phys. Commun. **181**, 2126 (2010)
40. C.E. Stone, A.C. Hannon, T. Ishihara, N. Kitamura, Y. Shirakawa, R.N. Sinclair, N. Umesaki, A.C. Wright, J. Non-Cryst. Solids **293-295**, 769 (2001)
41. X. Zhu, L. Chen, Physica B **404**, 4178 (2009)
42. L. Ting, H. Shiping, Z. Jiqin, Chem. Phys. Lett. **471**, 253 (2009)
43. M. Micoulaut, X. Yuan, L. Hobbs, J. Non-Cryst. Solids **353**, 1961 (2007)
44. E. Lorch, J. Phys. Chem. **2**, 229 (1969)
45. P. Salmon, Proc. R. Soc. Lond. A **445**, 351 (1994)
46. P. Vashishta, R.K. Kalia, J.P. Rino, I. Ebbsjö, Phys. Rev. B **41**, 12197 (1990)
47. L. Koester, H. Rauch, M. Herkens, K. Schröder, Summary of neutron scattering lengths, KFA Jülich Report Jül-1755, 1981
48. D.T. Cromer, J.T. Weber, in *International Tables for X-Ray Crystallography*, edited by J.A. Ibers, W.C. Hamilton (Kynoch Press, Birmingham, 1974), p. 71
49. M. Tokonami, Acta Cryst. **19**, 486 (1965)
50. R.J. Bell, Rep. Prog. Phys. **35**, 1315 (1972)
51. S. Davis, A.B. Belonoshko, B. Johansson, A. Rosengren, Phys. Rev. B **84**, 064102 (2011)